

Label-free intraoperative histology of bone tissue via deep-learning-assisted ultraviolet photoacoustic microscopy

Received: 6 September 2021

Accepted: 15 August 2022

Published online: 19 September 2022

 Check for updates

Rui Cao¹, Scott D. Nelson², Samuel Davis¹, Yu Liang³, Yilin Luo¹, Yide Zhang¹, Brooke Crawford⁴✉ and Lihong V. Wang¹✉

Obtaining frozen sections of bone tissue for intraoperative examination is challenging. To identify the bony edge of resection, orthopaedic oncologists therefore rely on pre-operative X-ray computed tomography or magnetic resonance imaging. However, these techniques do not allow for accurate diagnosis or for intraoperative confirmation of the tumour margins, and in bony sarcomas, they can lead to bone margins up to 10-fold wider (1,000-fold volumetrically) than necessary. Here, we show that real-time three-dimensional contour-scanning of tissue via ultraviolet photoacoustic microscopy in reflection mode can be used to intraoperatively evaluate undecalcified and decalcified thick bone specimens, without the need for tissue sectioning. We validate the technique with gold-standard haematoxylin-and-eosin histology images acquired via a traditional optical microscope, and also show that an unsupervised generative adversarial network can virtually stain the ultraviolet-photoacoustic-microscopy images, allowing pathologists to readily identify cancerous features. Label-free and slide-free histology via ultraviolet photoacoustic microscopy may allow for rapid diagnoses of bone-tissue pathologies and aid the intraoperative determination of tumour margins.

Approximately 18.1 million new cancer cases were diagnosed worldwide in 2018, while the number of new cancer cases per year is expected to rise to 29.5 million, with 9.6 million cancer-related deaths by 2040¹. Despite advances in cancer treatment, surgery remains the cornerstone, and more than 80% of cancer patients have a surgical procedure at some point in the cancer evolution^{2,3}. In oncologic surgery, intraoperative pathological examination provides surgical guidance and identification of tumour margins⁴. The border of the removed tissue in tumour surgery is often examined by intraoperative frozen section to ensure negative margins, meaning normal tissue surrounding the resected tumour⁵. Most localized tumours with negative margin

resection show much better outcomes and a lower chance of tumour recurrence. The intraoperative evaluation of tumour margins allows confirmation of complete tumour resection before oncologic surgeons close the surgical wound and helps patients avoid a second tumour resection surgery.

To provide rapid pathological examination and guide tumour resection, oncologic surgeons currently rely on the frozen section technique, which typically takes a small portion of tissue and freezes the tissue in a cryostat machine⁶. The frozen tissue is then cut into thin sections (5–8 μm) using a microtome or cryostat and stained for direct examination under a microscope. However, the need to section the

¹Caltech Optical Imaging Laboratory, Andrew and Peggy Cherng Department of Medical Engineering, Department of Electrical Engineering, California Institute of Technology, Pasadena, CA, USA. ²Department of Pathology, David Geffen School of Medicine at UCLA, Los Angeles, CA, USA. ³Department of Pathology, City of Hope, Duarte, CA, USA. ⁴Department of Orthopedic Surgery, David Geffen School of Medicine at UCLA, Los Angeles, CA, USA.

✉e-mail: brookecrawford@mednet.ucla.edu; lvw@caltech.edu

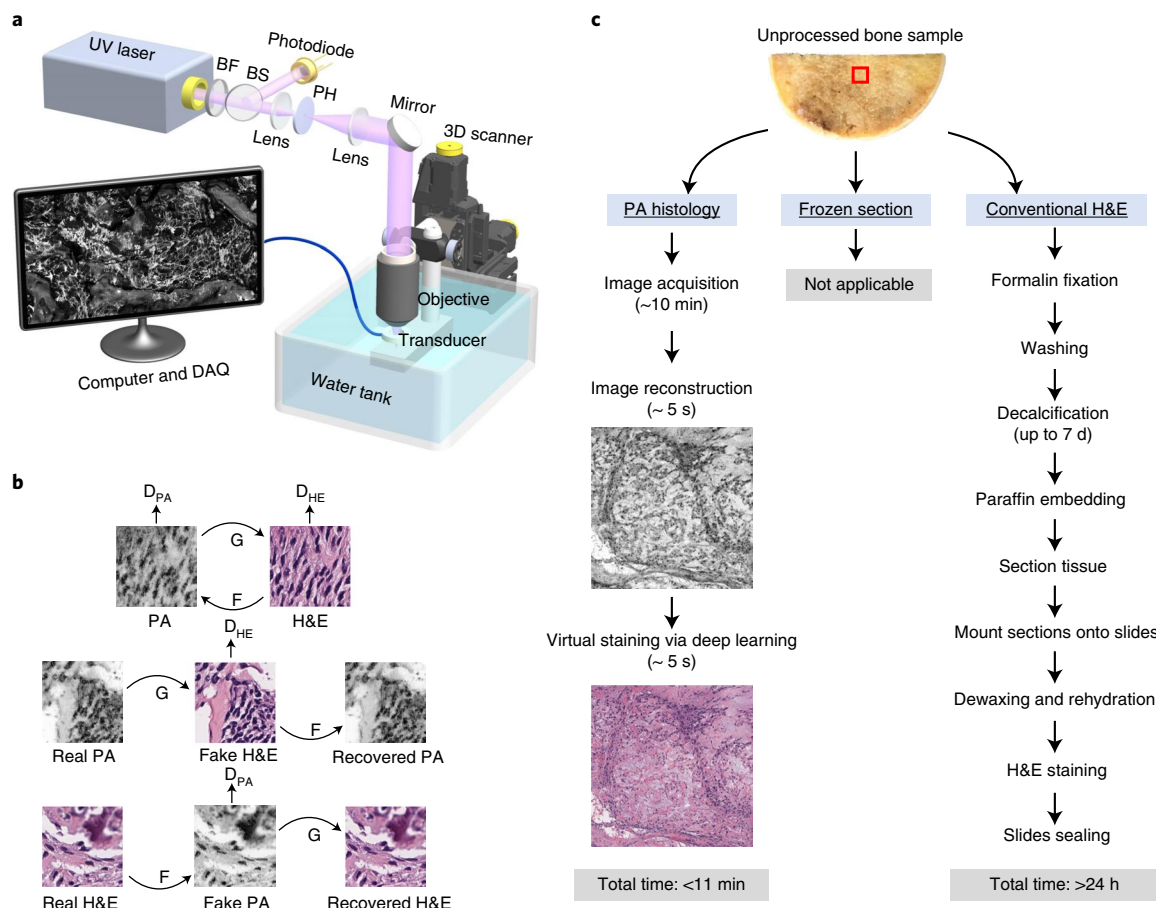


Fig. 1 | Rapid label-free UV photoacoustic histology via deep learning.

a, Schematic of the 3D contour scan UV-PAM system. The UV laser is spectrally filtered by a bandpass coloured glass filter (BF) and spatially filtered and expanded using a pair of lenses and a pinhole (PH). The beam sampler (BS) is placed before the lens to pick up a small fraction of the beam for photodiode measurement to compensate for the laser pulse-to-pulse energy fluctuation. The collimated and expanded beam is focused through a ring-shaped ultrasound transducer using a customized water-immersed objective and illuminates

the specimen for photoacoustic excitation. The 3D contour-scanning of the specimen placed on the sample holder is implemented for UV-PAM imaging. **b**, Deep-learning network architecture for virtual staining of PAM images. The CycleGAN model consists of two generators, G: PA→H&E and F: H&E→PA, and corresponding adversarial discriminators, D_{PA} and D_{HE} . **c**, The workflow for PA histology and conventional H&E staining histology of bone samples ($1 \times 1 \text{ mm}^2$ FOV).

specimen into thin slices prevents this technique from being used for hard tissue and may also cause inevitable tissue loss. For instance, the rapid pathological examination of calcified bone (cortical bone and calcified tumours) often cannot be evaluated by the frozen section technique due to the ossification^{7,8}. It is usually impossible to directly cut the undecalcified bone tissue into slices thin enough for traditional pathological examination. Instead, the bone must undergo a decalcification process that can take up to several days, which may introduce artefacts if under-decalcified or over-decalcified⁹.

The difficulties of rapid pathological examination of bone specimens have been a long-standing challenge for orthopaedic oncologists in medical practice. For orthopaedic oncologists resecting primary bone tumours, the need for time-consuming decalcification procedures often obviates pathological analysis during the operation. Thus, the surgeons tend toward wider margins based on pre-surgical imaging of bone tumours rather than intraoperative tissue analysis. Although wider margins are desirable for local tumour control, the functional loss can be much greater if those margins include vital structures such as tendons, nerves, blood vessels or joints. Many surgeons use 2 cm as the ideal bony margin and measure this off the pre-operative imaging, while a meta-analysis performed in 2019 showed that a 2 mm margin is sufficient to avoid local recurrence¹⁰. Since calcified primary

bone tumours, such as osteosarcoma, present most commonly in a periarticular location, 1.8 cm of margin difference could lead to joint salvage, increased patient bone stock for any future surgery needed and less morbidity¹⁰. A modality that allows for fast, accurate bony margin analysis would be an invaluable tool in limb-salvage surgery.

In recent years, rapid developments in imaging techniques have revolutionized many biological and biomedical areas as well as pathology. Multiple fluorescence microscopy methods have been demonstrated for diagnostic imaging, including confocal microscopy¹¹, wide-field structured-illumination microscopy (SIM)^{12,13}, light-sheet microscopy¹⁴ and microscopy with UV surface excitation (MUSE)¹⁵. However, these fluorescence microscopy techniques require dye staining of the specimen to provide image contrast, which involves complicated and different procedures for various samples before imaging and needs highly experienced personnel. Label-free optical imaging techniques have also been developed for rapid pathological diagnoses, such as stimulated Raman scattering microscopy (SRS)^{16,17} and coherence tomography/microscopy (OCT/OCM)^{18,19}. However, although MUSE and SRS techniques provide fast surface imaging of slide-free specimens, they lack depth-resolving capability and suffer from limited depth of field, resulting in blurred images of uneven surfaces with unprocessed slide-free specimens. The deconvolution-based

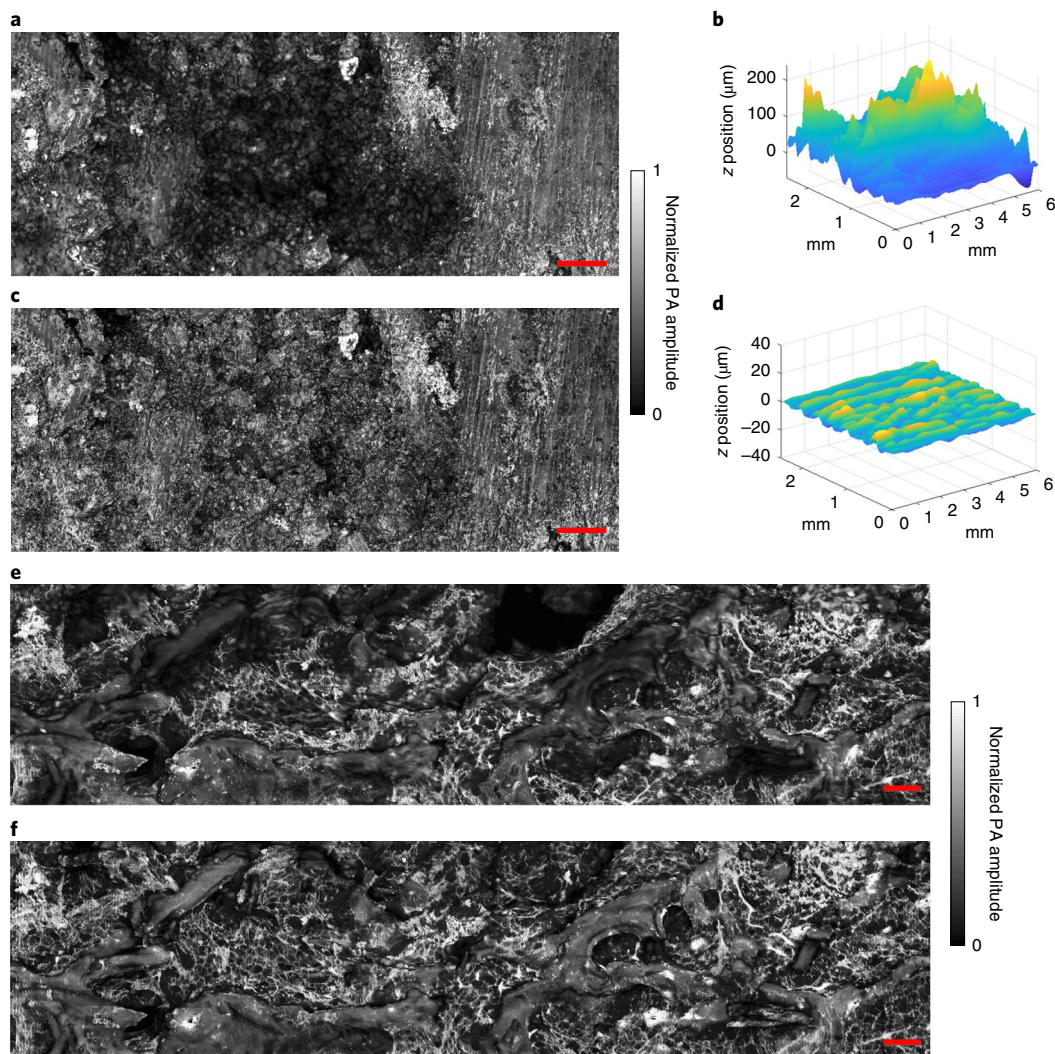


Fig. 2 | Label-free 3D contour-scanning UV-PAM of thick (>1 cm) unprocessed bone specimens. a–d, The UV-PAM images of the undecalcified left tibia bone extracted from a patient with osteofibrous dysplasia-like adamantinoma acquired by 2D raster-scanning (a) and 3D contour-scanning (c), showing the improved image quality by 3D contour-scanning of the undecalcified bone specimen with a rough surface. Scale bar, 500 μm . The profiles of the specimen

surface position in the axial direction relative to the optical focal plane during 2D raster-scanning (b) and 3D contour-scanning (d) are calculated by the time-of-flight information of the photoacoustic signal. **e, f,** A normal unprocessed thick bone sample is also imaged and compared using 2D raster-scanning (e) and 3D contour-scanning (f). Scale bar, 250 μm .

image fusion and multi-layer z-stacked images can be used to achieve an extended depth of field. However, it usually takes much longer imaging time, requires careful camera calibration and tedious experimental measurement of the point spread function, which are highly sensitive to noise or image variability²⁰. While OCT has depth-resolving capability, it cannot provide direct nuclear contrast within tissues since the optical scattering contrast does not have sufficient chromophore specificity²¹. Thus, OCT images cannot well match the current pathology standard of hematoxylin and eosin (H&E) staining in detail, which limits its application as a pathological diagnostic tool. A comparison of the different imaging modalities and traditional pathology approaches can be found in Supplementary Table 1.

Flatness is difficult to achieve in calcified bone tumours resected during operation, as cutting hard and calcified bone inevitably leads to rough surfaces. To address these challenges, we have developed the real-time three-dimensional (3D) contour-scan ultraviolet photoacoustic microscopy (UV-PAM) and demonstrated the label-free imaging of thick unprocessed bone, which requires minimal tissue preparation. The capability of imaging the non-sectioned bone specimen allows

direct visualization of well-preserved structure and composition of calcifications, which could make UV-PAM potentially an ideal tool for rapid diagnosis of challenging tissues such as thick calcified bone specimens. As a hybrid imaging modality, photoacoustic tomography (PAT) detects either endogenous or exogenous contrast-induced ultrasound signals through light absorption^{22,23}. The wavelength-dependent absorption allows PAT to quantitatively measure the concentration and distribution of different optical absorbers, while the less-scattering ultrasound detection enables high-resolution deep tissue imaging. The unique advantage of scalable spatial resolutions and imaging depths makes PAT attractive for various applications, ranging from imaging of nanometre-scale mitochondria to millimetre-level blood vessels in deep tissue²². Based on imaging resolution and reconstruction approaches, PAT can be implemented in the form of either photoacoustic computed tomography (PACT) or photoacoustic microscopy (PAM)²³. While PACT is mostly used for deep tissue imaging at the ultrasound resolution, PAM is often implemented with the optical diffraction-limited resolution. Utilizing the nonlinear absorption or Grüneisen parameter, PAM is also capable of achieving super-resolution

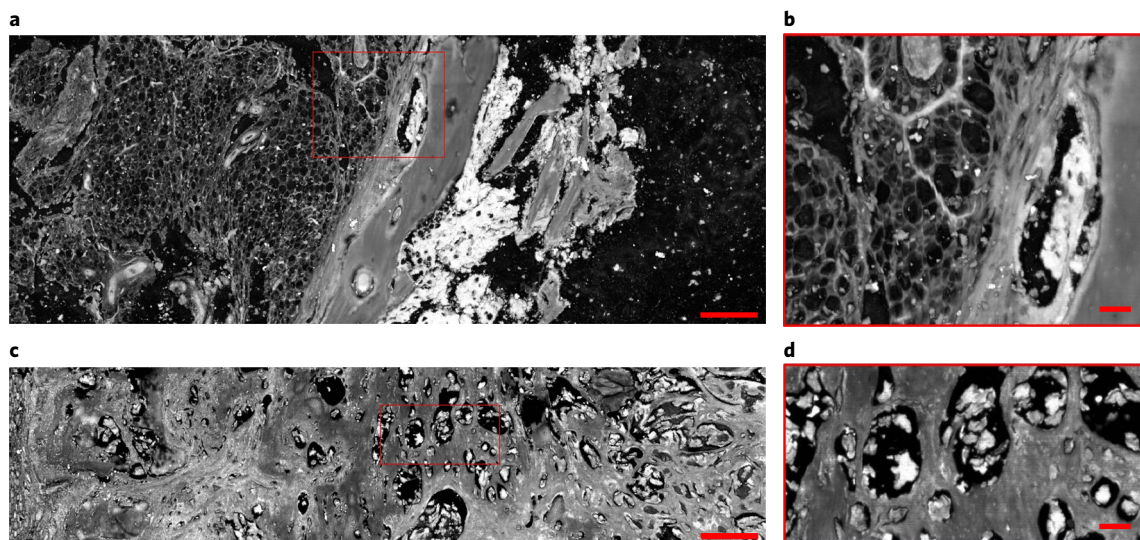


Fig. 3 | Label-free UV-PAM of decalcified bone specimens. **a**, PAM image of a FFPE decalcified non-neoplastic bone fragment on a glass slide. A near vertically oriented trabecula of cancellous bone is seen in the middle portion of the image. Scale bar, 500 μm . **b**, A close-up image of **a** showing a portion of the cancellous bone at the left border of the image. Scale bar, 100 μm . **c**, PAM

image of a FFPE decalcified bone specimen with metastatic poorly differentiated adenocarcinoma of pulmonary origin shows neoplastic glandular profiles of metastatic carcinoma on a glass slide. Scale bar, 500 μm . **d**, A close-up image of **c** shows nests and glandular profiles of metastatic carcinoma. Scale bar, 100 μm .

imaging beyond the optical diffraction limits^{24–26}. Depending on the illumination wavelength, various contrasts have been imaged by label-free PAM, including but not limited to haemoglobin^{27,28}, DNA/RNA²⁹, cytochrome³⁰, water³¹, lipid³² and protein³³.

In this study, we report the development of the UV-PAM system using a 266 nm nanosecond pulsed laser and show its use for the histology-like imaging of bone specimens. We implemented a real-time 3D contour-scanning mechanism to ensure consistent and optical diffraction-limited resolution for uneven bone specimen surfaces, which does not require previous knowledge of the surface profile. Using the UV-PAM system, we show histology-like imaging of unprocessed thick bone specimens with rough surfaces, which is challenging to carry out with traditional histological techniques. The UV-PAM images of both decalcified and undecalcified bone sections were acquired and compared with gold-standard H&E histology images for validation. In addition, we present an unsupervised deep-learning-based method for performing virtual H&E staining of greyscale UV-PAM images, to provide pathologists with complementary contrast and to help them interpret PAM images. Unlike supervised deep-learning methods such as generational adversarial networks (GAN)^{34,35}, our unsupervised deep-learning method based on cycle-consistent generational adversarial networks (CycleGAN) does not require coupled pairs of stained and unstained images^{36,37}. It avoids the need for well-aligned UV-PAM and H&E histology images for neural-network training, which can be challenging to acquire owing to artefacts caused by sample preparation-induced morphology changes.

Results

Histopathological examination of bone tissue via UV-PAM

With optical focusing and the time-of-flight information from photoacoustic (PA) signals, PAM images the contrast distribution in 3D. The PA signal is received by a 42 MHz ultrasound transducer and digitized by a data acquisition card sampling at 500 MHz. We found that PAM can localize the z positions of the sample surface with accuracy finer than the acoustical resolution ($\sim 40 \mu\text{m}$) by a factor of approximately 10 as limited by the signal-to-noise ratio. The UV-PAM employs a 266 nm nanosecond pulsed laser to image the DNA/RNA. While the penetration depth depends on the sample type, in bone specimens, we found that

the UV light penetration is less than the acoustical resolution. Thus, no deep PA signal is generated and mixed with surface signals, allowing direct imaging of the surfaces of thick bone specimens. While soft tissue can be sampled or squeezed with a flat surface, unprocessed hard tissues (that is, calcified primary bone; Supplementary Fig. 1) usually have a rough surface due to tissue extraction.

The 3D contour-scanning UV-PAM (Fig. 1a) allows direct imaging of thick specimens with rough surfaces, providing the possibility of rapid pathological diagnosis of undecalcified thick bone. Since the height differences in adjacent B-scan positions (0.625 μm away from each other) can be reasonably assumed to be much smaller than the depth of focus (DOF) of our UV-PAM ($\sim 9 \mu\text{m}$), the z contour-scanning trajectory can be predicted and updated in real time after the first seed B-scan for the full field of view (FOV), without previous knowledge of the surface contour (Supplementary Fig. 2). Thus, the real-time 3D contour-scanning UV-PAM can ensure that the distance between the image position and the focal plane is within the DOF, resulting in a consistent diffraction-limited lateral resolution for rough surface imaging. The performance of the proposed contour-scanning mechanism has been tested using a phantom with a bent black tape, which showed well-compensated distances in the full FOV (Supplementary Fig. 3a–c). The measured lateral resolution is 0.96 μm (Supplementary Fig. 3d).

After acquiring a greyscale UV-PAM image of the sample surface, the unsupervised deep learning method based on CycleGAN is used to implement the virtual staining. The deep-learning network architecture (Fig. 1b) for virtual staining consists of two generators (G and F) and corresponding adversarial discriminators (D_{PA} and D_{HE}). Each pair of generators and discriminators are trained so that the outputs of G and F are indistinguishable from real PAM and H&E histology images, respectively. The generators are further regularized using the cycle-consistency loss—transforming an image from one domain and back should recover the original input. This process ensures that the transformations are bijective and produce corresponding morphology. The combination of cycle consistency and discriminator loss terms avoids the necessity for well-aligned paired datasets, which are needed in traditional l_2 -norm or similar loss training between a network output and a target label. With the neural network well trained, it takes less than 5 s to virtually stain an image of $1,600 \times 1,600$ pixels.

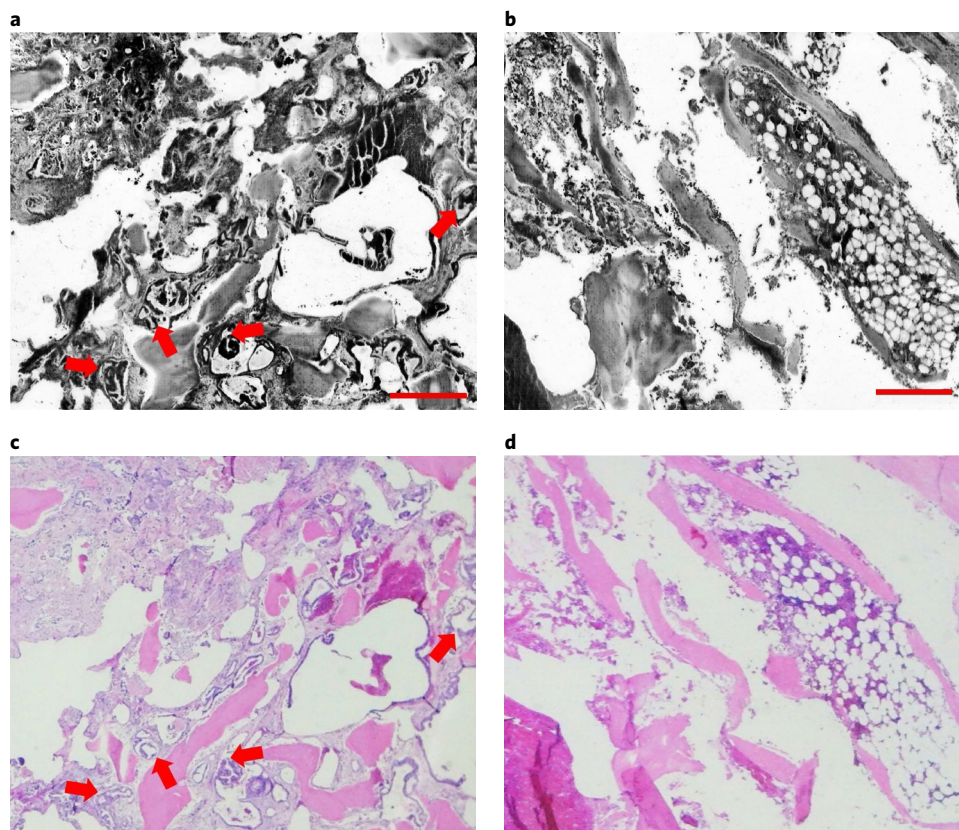


Fig. 4 | Label-free UV-PAM for identifying tumours in decalcified bone fragments. **a**, PAM image of a decalcified bone section on a glass slide with metastatic adenocarcinoma. **b**, PAM image of a decalcified bone section on a glass slide with normal bone fragment and hematopoietic marrow. The PAM

contrast is reversed to highlight the high-absorption region in dark color for better comparison. **c,d**, Corresponding H&E images of **a** and **b**. Neoplastic glands of metastatic carcinoma among bone fragments are indicated by red arrows in **a** and **c**. Scale bars, 500 μm .

Thanks to the real-time 3D contour-scanning UV-PAM system and deep-learning-assisted virtual staining, the rapid diagnosis of unprocessed bone becomes possible. The workflows of both PA histology and traditional H&E histology of bone clearly reveal the advantage of PA histology (Fig. 1c). While the frozen section technique is not applicable to hard bone specimens, conventional H&E histology techniques for bone can take up to 7 days. In contrast, the PA histology technique can produce virtually stained images of unprocessed bone for pathological examination within 11 min (0.625 μm step size, $1 \times 1 \text{ mm}^2$ FOV).

3D contour-scanning UV-PAM of thick patient bones

To demonstrate the imaging of unprocessed thick bone specimens for rapid pathological diagnosis, we extracted mineralized primary bone specimens from patients in a tumour resection surgery. Unprocessed bone specimens were immediately fixed in the formalin solution after surgical excision to prevent degradation. No further cutting or sectioning was implemented with the bone specimen, avoiding the need for paraffin or agarose embedding. Then, the bone specimen was placed onto a customized water-immersed sample holder for scanning. We obtained the left tibia bone specimens from a patient with osteofibrous dysplasia-like adamantinoma, which has a rough surface due to the surgical excision by an oscillating saw. The image acquired by 2D raster-scanning without contour compensation (Fig. 2a) shows a large portion of the out-of-focus area within the FOV ($2.5 \times 6.25 \text{ mm}^2$), resulting in an inconsistent resolution and poor image quality. The rough bone surface profile is reconstructed by the PA signal time-of-flight information (Fig. 2b), revealing large fluctuation in surface height and less than 10% of the pixels within the DOF. In contrast, the UV-PAM image acquired by 3D contour-scanning of the same area showed an

improved image quality and consistent resolution across the FOV (Fig. 2c). More than 92% of the surface area is within the small DOF during the 3D contour-scanning (Fig. 2d). Another comparison between the 2D raster-scanning PAM image and the 3D contour-scanning PAM image of unprocessed patient bone can be found in Fig. 2e,f. As shown in Fig. 2f, important bone structures, such as trabeculae and marrow, can be visualized by UV-PAM with specimen integrity. More 3D contour-scanning UV-PAM demonstrations of undecalcified thick bone specimens can be found in Supplementary Figs. 4 and 5. It clearly shows that the 3D contour-scanning UV-PAM system is capable of imaging the rough surfaces of unprocessed thick bone specimens. In contrast, it is difficult to acquire high-quality images using the traditional 2D raster-scanning approach. Since UV-PAM imaging is non-destructive, the unprocessed bone specimens can be used for further pathological diagnosis.

H&E validation for label-free UV-PAM of bone specimens

Since the traditional H&E histology slice of bone usually requires decalcification and cutting into thin sections (that is, 5–8 μm), we first demonstrated UV-PAM imaging of a formalin-fixed paraffin-embedded (FFPE) decalcified bone fragment without malignancy on a glass slide. As shown in Fig. 3a,c, obvious bone structures, including decalcified mineralized bone, can be readily visualized. In addition, the close-up images (Fig. 3b,d) demonstrate profiles and nests of metastatic carcinoma within the medullary space of the bone. The decalcified bone specimen from the patient with chondroblastic osteosarcoma is also imaged by UV-PAM and shown in Supplementary Fig. 6.

To validate the PA histology of bone fragments, we compared UV-PAM images of both decalcified and undecalcified bone specimens with gold-standard H&E histology images acquired by a traditional

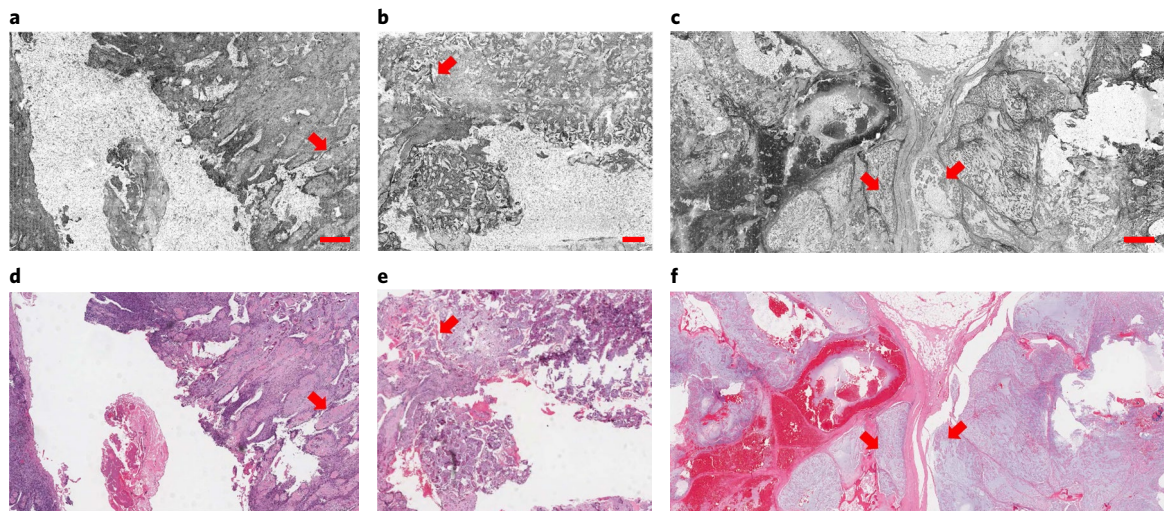


Fig. 5 | Label-free UV-PAM of undecalcified bone specimen and H&E validation. **a, b**, UV-PAM images of undecalcified patient bone sections on a glass slide from patient #1 with osteoblastic osteosarcoma showing neoplastic osteoid matrix—the lacy material in between the nuclei of the neoplastic cells, denoted by red arrows. **c**, UV-PAM images of an undecalcified patient bone section on a

glass slide from patient #2 with chordoma, demonstrating lobules of the myxoid tumour, denoted by red arrows. **d–f**, Corresponding H&E images acquired by a digital whole-slide scanning microscope with a $\times 40$ objective, with an essentially identical appearance. Scale bars, 500 μm .

optical microscope. Here, the contrast of PAM images is reversed to highlight the high-absorption region in dark colour for better comparison with H&E histology images. A comparison between the original greyscale image and the image in reversed contrast can be found in Supplementary Fig. 7. The decalcified bone section on a glass slide extracted from a patient with metastatic adenocarcinoma was imaged by UV-PAM (Fig. 4a) and compared with its corresponding H&E histology image (Fig. 4c). The UV-PAM image demonstrates the key features present in the H&E histology image, in which abnormal tumour glands are readily observable (indicated by arrows). Meanwhile, the PAM image of decalcified fragments of bone and hematopoietic marrow with no evidence of metastatic carcinoma (Fig. 4b) also shows the same structure as its corresponding H&E result (Fig. 4d). Furthermore, the undecalcified bone slices were imaged by PAM and compared with H&E histology images, to avoid potential artefacts that might be introduced by the decalcification procedures. Since these specimens were collected from a portion of the tumour with low calcification, they did not require the decalcification procedure to section the specimen into thin slices. The PAM images (Fig. 5a–c) of undecalcified bone sections on a glass slide are presented in reverse contrast. Figure 5a,b demonstrate features of osteoblastic osteosarcoma, while Fig. 5c demonstrates the myxoid lobules of chordoma. The corresponding H&E histology images were acquired by the digital whole-slide scanning microscope with a $\times 40$ objective (Fig. 5d–f) and show essentially identical structures as the PAM images. Close-up images in sliding windows are shown in Supplementary Video 1. Another example of UV-PAM and H&E comparison can be found in Supplementary Fig. 8, which was from a decalcified bone slice with high-grade osteosarcoma from the femur. The necrotic tumour (Supplementary Fig. 8b) and the viable tumour (Supplementary Fig. 8c,d) can be identified using the PAM images, which also show comparable features as the H&E histology images (Supplementary Fig. 8f,g).

Photoacoustic virtual histology via deep learning

To match traditional histologic images, we performed virtual H&E staining on the greyscale PAM images using a CycleGAN-based deep-learning method³⁶. The virtual staining CycleGAN network architecture is shown in Fig. 6. More detailed procedures of generating virtually H&E-stained PAM images are described in Methods. The

example UV-PAM images of the bone section are shown in greyscale contrast (Supplementary Fig. 9) and in histology-like pseudocolour (Fig. 7a,c), which demonstrate architectural features as well as cellular details similar to the corresponding H&E images (Fig. 7b,d). The close-up virtual histologic PAM images (Fig. 7a(i,ii),c(i,ii)) clearly show histologic features that would be important in the interpretation of pathological examination and that correspond to the close-up H&E images (Fig. 7b(i,ii),d(i,ii)). The virtual histologic images have been reviewed by three pathologists and one orthopaedic surgeon, who confirmed the comparable and interpretable histologic features present in the H&E histology slides that might be used for clinical diagnosis. More details of close-up images from the virtually stained PAM images and corresponding H&E histology images are shown in Supplementary Videos 2 and 3 for side-by-side comparison. The cell nuclear counts, nuclear cross-sectional areas and internuclear nearest-neighbour distances are quantitatively compared in Supplementary Fig. 10 and Table 2, demonstrating a good match between the virtual-staining photoacoustic image and the corresponding real H&E histology image. As shown in Supplementary Table 2, internuclear distances in two images match within the errors. The cell counts and nuclear cross-sectional areas are slightly different, which is expected as we were looking at neighbouring sections taken at different axial positions instead of the same section.

Discussion

The development of 3D contour-scanning UV-PAM in reflection mode enables more rapid pathological examination of bone specimens. In contrast, traditional pathological examination techniques for bone involve time-consuming decalcification procedures, and the frozen-section technique is often not applicable. With the bone mineral as its major component, dense cortical bones can take days to decalcify before it is soft enough to be sectioned into thin slices, which prevents rapid intraoperative diagnosis. Currently, orthopaedic surgeons heavily rely on pre-operative X-ray CT or magnetic resonance imaging to identify the extent of the tumour for the planning of resection margins. However, these imaging modalities cannot provide accurate diagnosis and intraoperative confirmation of tumour margins. The reflection-mode contour-scanning UV-PAM enables label-free imaging of unprocessed thick bone samples with rough surfaces, providing detailed information

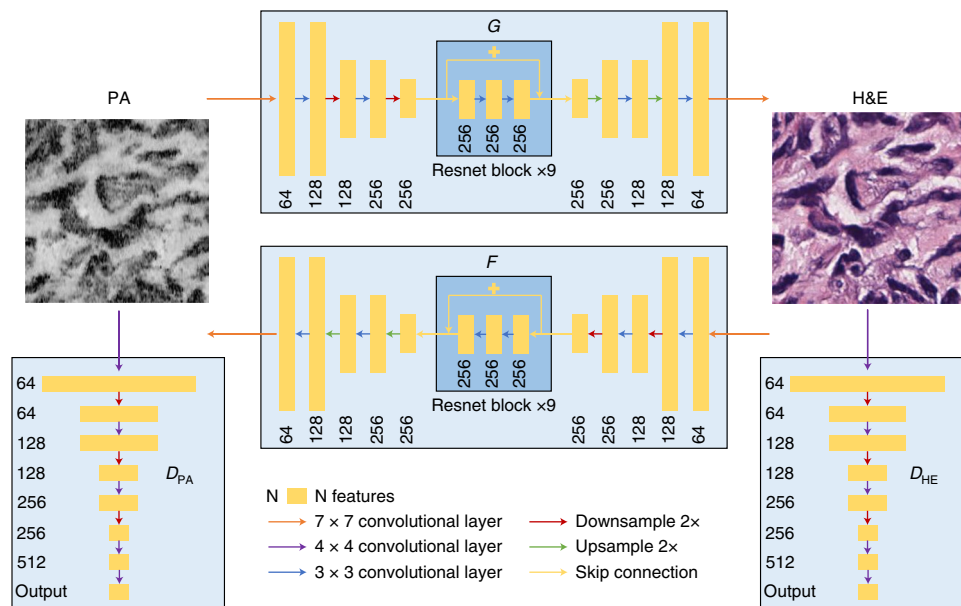


Fig. 6 | Detailed network architecture for virtual staining. The CycleGAN model consists of two generators, G: PA \rightarrow HE and F: HE \rightarrow PA, and corresponding adversarial discriminators, D_{PA} and D_{HE} . Each generator is composed of two downsampling blocks (a convolutional layer and an anti-alias downsampling layer of stride two), nine residual blocks (two convolutional layers and a skip connection) and two upsampling blocks (an anti-alias upsampling layer of

stride two and a convolutional layer). Each convolutional layer is followed by instance normalization and rectified linear unit (ReLU) activation layers. The discriminators are composed of three downsampling blocks, followed by an output convolutional layer. Each convolutional layer in the discriminators is followed by instance normalization and leaky ReLU activation layers. The network is applied to image patches of 256×256 pixels.

for rapid pathological examination of the tumour margin, meeting a critical need for intraoperative margin analysis.

When rendering a diagnosis from standard H&E histology slides, pathologists examine the architecture morphology and cellular features such as cell nuclei, cytoplasm and extracellular matrix. The H&E staining approach has been widely used for a long time in histology, as it provides a clear contrast between cell nuclei and cytoplasmic parts by staining them in different colours. Thus, pathologists are accustomed to the stained and counterstained appearance of H&E histology tissue samples, which show extracellular matrix and cytoplasm as pink, and cell nuclei as blue/purple. At the UV wavelength of 266 nm³⁸, cell nuclei have much higher absorption coefficient and PA amplitudes than the extracellular matrix and cytoplasm, allowing their virtual labelling in different colours similar to H&E staining. We processed greyscale PAM images and generated pseudocolour images for virtual H&E staining by applying the deep-learning approach with CycleGAN, which does not need well-aligned PAM and H&E histology image pairs for neural-network training. The virtually stained pseudocolour PAM images demonstrated cellular, nuclear and cytoplasmic detail matching the corresponding H&E histology images. With more clinically relevant PAM virtual histology results, the deep convolutional neural-network technique may be further used to potentially achieve automatic diagnosis and tumour margin detection¹⁶.

Although we have demonstrated the potential of UV-PAM for rapid diagnosis of unprocessed bone specimens, further improvements can be made toward better clinical use. One key challenge is to improve the image speed to allow for faster intraoperative feedback. The current UV-PAM system employs a pulsed 266 nm laser with a pulse repetition rate of up to 50 kHz, which limits the theoretical image speed to an A-line rate of 50 kHz. However, due to the accuracy and stability of step motors, it is challenging to ensure a good image quality of UV-PAM at high motor speeds. The current system is running at 10 kHz laser repetition rate, which takes about 10 min in practice to scan an FOV of $1 \times 1 \text{ mm}^2$ at the step size of $0.625 \mu\text{m}$. To achieve higher imaging speeds, we can use faster optical scanning

approaches and even higher laser repetition rates³⁹. Moreover, multichannel parallel imaging can be used to further boost the imaging speed, where multiple focal spots and an ultrasound transducer array are used for image reconstruction. For instance, a microlens array can be utilized to create multiple focal spots for multichannel parallel imaging, which has been reported to improve the imaging speed of UV-PAM by 40 times⁴⁰. However, the limited numerical aperture and the short working distance of the microlens array can only be used in transmission-mode UV-PAM, which impedes its practical use for high-resolution images of thick unprocessed biological samples. Reflection-mode multichannel UV-PAM with high resolution will be needed for faster intraoperative diagnosis.

Due to the physical limit of z-motor mechanical movement, which cannot adjust position fast enough, a small portion (for example, $\sim 6.3\%$ in Fig. 2c) of the areas may still fall out of the DOF if we scan a large FOV (for example, $6 \times 8 \text{ mm}^2$). To further improve the performance of high-resolution PAM imaging of rough surfaces, an electrically tunable lens may be integrated into our system to allow faster optical focus shifting with high accuracy⁴¹. Since the acoustical DOF of the focused ultrasonic transducer is often much longer (that is, hundreds of microns) than the optical DOF, the optical focus shifting within the acoustic DOF can be used to compensate for the steep height fluctuation, while the time-dependent gain compensation technique can be used to compensate for the transducer sensitivity difference within the acoustic DOF⁴².

Compared with traditional intraoperative pathological methods (that is, freeze sectioning), photoacoustic histology can lower costs by reducing the turnaround time and avoiding highly specific personnel for sample preparation and specimen transportation. It may also enable remote and automatic pathological diagnostics in the future. The current UV-PAM system employs a Q-switched neodymium-doped yttrium lithium fluoride (Nd:YLF) nanosecond pulsed UV laser at a wavelength of 266 nm to generate photoacoustic signals of cell nuclei, which may be challenging for in vivo imaging due to the safety concern of UV laser. The need for nanosecond pulsed UV laser increases the cost of the PAM

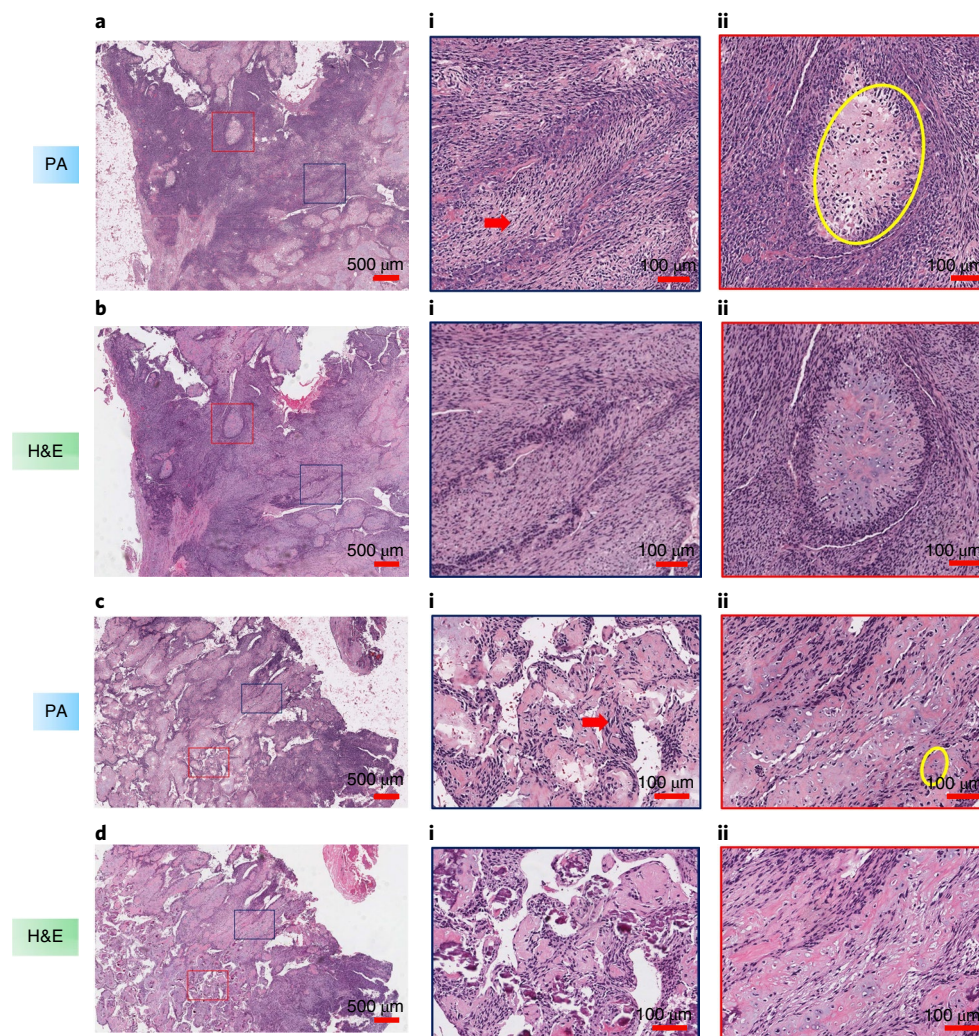


Fig. 7 | Label-free UV-PAM virtual histology of undecalcified bone via unsupervised deep learning. **a,c**, Virtual-stained PAM images of undecalcified bone sections on a glass slide. **b,d**, Corresponding H&E histology images. In **a**, close-up images show neoplastic spindle cells (denoted by many long, spindle-shaped purple nuclei, red arrow) arranged in vague streaming and fascicular patterns (**i**), and a nodule of neoplastic chondroid material (**ii**, yellow circle),

corresponding to H&E histology images in **b(i),(ii)**. In **c**, close-up images show ribbons of neoplastic spindle cells (**i**, red arrow) and disorganized osteoid, the streaky bands denoted by the yellow circle (**ii**), corresponding to the H&E histology images in **d(i),(ii)**. Scale bars, 500 μm (**a–d**), 100 μm (in all closed-up images).

system. Further developments using longer laser wavelengths for photoacoustic histological imaging will not only enable *in vivo* imaging but also significantly lower equipment cost. Another limitation is that the current system requires specimens to be mounted onto a sample holder and immersed in water for mechanical scanning and acoustic coupling, which is suboptimal for high-throughput histological imaging. A better configuration that allows the specimen to be outside the water tank will ensure even easier sample handling for rapid high-throughput histological imaging.

In summary, we have shown that label-free UV-PAM is a valid method for imaging unprocessed bone without the need for tissue sectioning. The immediate clinical indication for these results is to possibly provide rapid pathological examination of bone tumour margins. Because no physical sectioning is needed, it does not require highly specific trained technicians for bone-specimen preparation. Moreover, the undestroyed bone specimen can be further examined by other techniques after label-free UV-PAM imaging. Although in this work we have focused on bone, which is one of the most challenging biological tissues in rapid pathological diagnosis, the imaging system can also be applied to other types of specimens. We believe it could

aid pathological diagnosis and provide immediate feedback for the intraoperative determination of tumour margins.

Methods

All experiments and protocols in this study were approved by the Institutional Review Boards at the California Institute of Technology, the University of California at Los Angeles and the City of Hope.

Label-free reflection-mode UV-PAM

The reflection-mode UV-PAM system used an Nd:YLF Q-switched 266 nm nanosecond pulsed laser (QL266-010-O, CrystaLaser). A band-pass glass filter (FGUV5, Thorlabs) was placed at the laser output to reject the leaked pump light. After passing the coloured glass filter, a small portion of the beam was reflected by a UV-fused silica beam sampler (BSF10-UV, Thorlabs) and directed to a Si photodiode (PDA36A, Thorlabs) for pulse-to-pulse fluctuation compensation. The UV laser beam was expanded by a pair of plano-convex lenses and spatially filtered by a 15 μm high-energy pinhole (900PH-15, Newport). The expanded and collimated beam was then focused onto the sample by a custom-made water-immersion UV objective lens (consisting of an

aspheric lens, a concave lens and a convex lens (NT49-696, NT48-674, NT46-313, Edmund Optics)) with a numerical aperture of 0.16. A customized ring-shaped ultrasonic transducer (42 MHz centre frequency, 76% –6 dB two-way bandwidth) with a central aperture was used to detect the PA signal, which allows optical and acoustical confocal alignment. The detected signal was amplified by two low-noise amplifiers (ZFL-500LN+, Mini-Circuits) and digitized by a data acquisition card (ATS9350, Alazar Technologies) at a 500 MHz sampling rate. The PAM image was acquired by scanning the water-immersed sample mounted onto a customized 3D scanner (consisting of three step motors, PLS-85, PI Micos). The reconfigurable I/O device (myRIO-1900, National Instruments) with a field-programmable gate array was used to control and synchronize laser pulses, motor movements and data acquisition.

Real-time 3D contour-scanning UV-PAM

To allow imaging of the rough surface of unprocessed thick samples like bone, we developed the contour-scanning mechanism without previous knowledge of the sample surface using a 3-axis motorized stage, which ensures consistent lateral resolution within a large field of view. For consistent and optimized optical resolution, the distance between the sample and optical focus should be maintained within the DOF during scanning. In contour scanning, the time-of-flight information of PA signals was used to calculate the distance between the sample and the focal spot, which could be adjusted by the z-motor during scanning. With the numerical aperture of 0.16, the DOF of our UV-PAM microscope was only about 9 μm , which corresponds to 6 ns ultrasound propagation for a speed of sound of 1,500 m s^{-1} at room-temperature water. The acquired PA signal was digitized at the sampling rate of 500 MHz (ATS9350, AlazarTech). The z-profile of the sample surface could be accurately calculated using the time-of-flight information of PA signals, enabling contour scanning for z-position compensation.

Before PAM imaging, the optical and acoustic foci were confocally aligned, while the propagation time of the acoustic signal from the optical focus was recorded to determine the focal spot position. To extract the ultrasound propagation time, we calculated the centres of positive and negative peak positions in PA A-line signals, which were converted to the sample position. Without previous knowledge of the sample surface profile, one seed B-scan with the z-motor disabled was implemented to calculate the starting contour trajectory. To avoid potential noise interference and remove outliers, a 100-point moving average was used to generate a smooth z-scanning trajectory. During the contour scanning, both the x-axis and the z-axis motors moved simultaneously. After the first contoured B-scan, the z-motor trajectory and the distance between the sample surface and the ultrasonic transducer were calculated and used to compute the accurate surface profile. Due to the small y step (0.625 μm), we set the second z-motor trajectory to follow the surface profile from the previous contoured B-scan⁴³. Then, the surface profile was updated according to the second contoured B-scan. This process was repeated until the whole scanning was completed. Real-time data processing and system control were implemented using MATLAB and LabVIEW hybrid programming.

Bone specimen preparation and H&E imaging

The bone specimens for UV-PAM imaging were procured, with the informed consent of patients, from larger specimens in the pathology laboratory, the specimens having been surgically removed from patients at the City of Hope and the UCLA medical centre. All bone specimens were fixed in 10% buffered formalin before any other procedures. For thick undecalcified specimens in this study, the specimens were mounted to the sample holder for imaging without further processing. To decalcify specimens, we treated the bone specimens with a decalcifying solution containing chelating agents in dilute HCl, with the treatment time varying depending on the size and hardness of the specimens. After fixation and decalcification, the specimen was embedded in paraffin wax, sectioned into 5- μm -thick slices and placed on

glass slides. Specimens with less calcification were sectioned without decalcification. These slices were then processed with standard H&E staining and cover-slipped. The H&E histology slides were imaged using either the standard optical microscope or the digital whole-slide scanning microscope (Leica Aperio AT2) with a $\times 40$ objective.

UV-PAM virtual histology via CycleGAN

To reconstruct the UV-PAM images, we first calculated the PA amplitude of each A-line signal after the Hilbert transform. The pulse energy measured by the photodiode was used to normalize the PA amplitude and compensate for the laser pulse fluctuation. The axial position of the specimen surface was calculated by detecting the peak of the A-line signal after the Hilbert transform. The 2D maximal amplitude projection image was self-normalized. Since the PA amplitude of the contrast is proportional to its absorption coefficient, it can be used to effectively differentiate cell nuclei, cytoplasm and the background. The cell nuclei have the largest absorption coefficient at 266 nm and the highest PA signals. After calculating the greyscale UV-PAM, we used a trained neural network to perform virtual H&E staining, which is more familiar to pathologists and thus easier for them to interpret.

We used the CycleGAN architecture³⁶, shown in Fig. 6, which can learn how to map images from the UV-PAM domain, PA, to the H&E domain, HE, without the need for well-aligned image pairs. We used an adversarial loss to learn the transformations $G: \text{PA} \rightarrow \text{HE}$ and $F: \text{HE} \rightarrow \text{PA}$, such that the images $G(\text{PA})$ and $F(\text{HE})$ are indistinguishable from HE and PA, respectively. The discriminators were trained to distinguish between real images and those produced by the generators. The loss function for D_{HE} is given by⁴⁴

$$l^{D_{\text{HE}}} = D_{\text{HE}}(G(\text{PA}))^2 + (1 - D_{\text{HE}}(\text{HE}))^2, \quad (1)$$

where PA is a UV-PAM image patch, and HE is an H&E histology image patch. Similarly, the loss function for D_{PA} is given by

$$l^{D_{\text{PA}}} = D_{\text{PA}}(F(\text{HE}))^2 + (1 - D_{\text{PA}}(\text{PA}))^2. \quad (2)$$

The generators were trained to try and fool the discriminators by producing images that match the statistical properties of the target domain. To ensure that G does not simply produce convincing but irrelevant H&E images, an additional loss term is necessary. Conventionally, this would be the l_2 or l_1 norm loss between the network output and some known ground-truth image. However, this requires well-aligned paired datasets, which are challenging to acquire after sample preparation.

Instead, the CycleGAN architecture learns the inverse transformation so that cycle consistency can be used to ensure that the images are of the same structures. The total loss for the generators is

$$l^G = (1 - D_{\text{HE}}(G(\text{PA})))^2 + (1 - D_{\text{PA}}(F(\text{HE})))^2 + \lambda |F(G(\text{PA})) - \text{PA}| + \lambda |G(F(\text{HE})) - \text{HE}|, \quad (3)$$

where the regularization parameter λ is set to 10.

The generators are residual networks consisting of an input convolutional layer, two convolutional layer and downsampling blocks, nine residual network blocks, two convolutional and upsampling blocks and, finally, an output convolutional layer⁴⁵. Instance normalization and ReLU layers were used after each convolutional layer. For the discriminator, we used PatchGAN consisting of convolutional layer and downsampling blocks, which classify whether the image is real on overlapping 70×70 pixel image patches⁴⁶. This patch size is a compromise between promoting high spatial frequency fidelity and avoiding tiling artefacts. In the discriminator networks, instance normalization and leaky ReLU (lReLU) layers, $\text{lReLU}(x) = \max(0.2x, x)$, were used after each convolutional layer. Anti-alias downsampling and upsampling layers were used in both the generators and discriminators to improve

shift invariance⁴⁷.

The training dataset consisted of UV-PAM images of undecalcified bone specimens. These images were converted into 17,940 and 26,565 286 × 286 pixel image patches for UV-PAM and H&E histology, respectively. During training, these were further randomly cropped to 256 × 256 for data augmentation. The training was performed with the Adam solver, with a batch size of 4 and an initial learning rate of 0.0002, decaying to zero over 100 epochs⁴⁸. Once trained, we used the generator *G* to transform UV-PAM data into overlapping 256 × 256 pixel image patches, which were recombined with linear blending. To validate the virtual histology performance, we quantitatively assessed the accuracy of our virtual staining method. We segmented the cell nuclei in comparative regions of interest to compare their numbers, sizes and densities. The nuclear segmentation was performed via Qupath⁴⁹, using the default cell detection settings with the threshold set to 0.3 to reduce false positives. The cell counts, average nuclear areas and average nearest-neighbour internuclear distances were calculated for comparison of the UV-PAM virtual histology and H&E results.

Reporting summary

Further information on research design is available in the Nature Research Reporting Summary linked to this article.

Data availability

The main data supporting the findings of this study are available within the paper and its Supplementary Information. The training dataset and the fake output images for the CycleGAN network are available at <https://doi.org/10.5281/zenodo.6345772>. The raw data generated during the study are too large to be publicly shared, yet they are available for research purposes from the corresponding authors on reasonable request.

Code availability

The original code for CycleGAN is available at <https://github.com/junyanz/pytorch-CycleGAN-and-pix2pix>. We applied this code to our dataset with the customized settings described in Methods. MATLAB was used for creating image tiles for the network and for restitching the output image tiles. The quantitative analysis of photoacoustic virtual histology was done via QuPath (<https://qupath.github.io>). The system control software and the data collection software are proprietary and used in licensed technologies.

References

1. Global Cancer Observatory (WHO, accessed 19 May 2021); <http://gco.iarc.fr/today/home>
2. Wyld, L., Audisio, R. A. & Poston, G. J. The evolution of cancer surgery and future perspectives. *Nat. Rev. Clin. Oncol.* **12**, 115–124 (2015).
3. Sullivan, R. et al. Global cancer surgery: delivering safe, affordable, and timely cancer surgery. *Lancet Oncol.* **16**, 1193–1224 (2015).
4. Mahe, E. et al. Intraoperative pathology consultation: error, cause and impact. *Can. J. Surg.* **56**, E13–E18 (2013).
5. DiNardo, L. J., Lin, J., Karageorge, L. S. & Powers, C. N. Accuracy, utility, and cost of frozen section margins in head and neck cancer surgery. *Laryngoscope* **110**, 1773–1776 (2000).
6. Brender, E., Burke, A. & Glass, R. M. Frozen section biopsy. *JAMA* **294**, 3200 (2005).
7. Campanacci, M. *Bone and Soft Tissue Tumors: Clinical Features, Imaging, Pathology and Treatment* (Springer, 2013).
8. *Pathology and Genetics of Tumours of Soft Tissue and Bone* (IARC, WHO, 2002).
9. Taqi, S. A., Sami, S. A., Sami, L. B. & Zaki, S. A. A review of artifacts in histopathology. *J. Oral Maxillofac. Pathol.* **22**, 279 (2018).
10. Gomez-Bouchet, A. et al. Assessment of resection margins in bone sarcoma treated by neoadjuvant chemotherapy: literature review and guidelines of the bone group (GROUPOS) of the French sarcoma group and bone tumor study group (GSF-GETO/RESOS). *Orthop. Traumatol. Surg. Res.* **105**, 773–780 (2019).
11. Gareau, D. S. et al. Confocal mosaicing microscopy in Mohs skin excisions: feasibility of rapid surgical pathology. *J. Biomed. Opt.* **13**, 054001 (2008).
12. Wang, M. et al. Gigapixel surface imaging of radical prostatectomy specimens for comprehensive detection of cancer-positive surgical margins using structured illumination microscopy. *Sci. Rep.* **6**, 27419 (2016).
13. Wang, M. et al. High-resolution rapid diagnostic imaging of whole prostate biopsies using video-rate fluorescence structured illumination microscopy. *Cancer Res.* **75**, 4032–4041 (2015).
14. Glaser, A. K. et al. Light-sheet microscopy for slide-free non-destructive pathology of large clinical specimens. *Nat. Biomed. Eng.* **1**, 0084 (2017).
15. Fereidouni, F. et al. Microscopy with ultraviolet surface excitation for rapid slide-free histology. *Nat. Biomed. Eng.* **1**, 957–966 (2017).
16. Hollon, T. C. et al. Near real-time intraoperative brain tumor diagnosis using stimulated Raman histology and deep neural networks. *Nat. Med.* **26**, 52–58 (2020).
17. Orringer, D. A. et al. Rapid intraoperative histology of unprocessed surgical specimens via fibre-laser-based stimulated Raman scattering microscopy. *Nat. Biomed. Eng.* **1**, 0027 (2017).
18. Assayag, O. et al. Large field, high resolution full-field optical coherence tomography: a pre-clinical study of human breast tissue and cancer assessment. *Technol. Cancer Res. Treat.* **13**, 455–468 (2014).
19. Nguyen, F. T. et al. Intraoperative evaluation of breast tumor margins with optical coherence tomography. *Cancer Res.* **69**, 8790–8796 (2009).
20. Fereidouni, F., Tracy, J. & Levenson, R. M. D. MUSE microscopy for thick tissue imaging with extended depth of field. In *Proc. SPIE 10489, Optical Biopsy XVI: Toward Real-Time Spectroscopic Imaging and Diagnosis 104890H* (SPIE, 2018).
21. Gambichler, T. et al. Comparison of histometric data obtained by optical coherence tomography and routine histology. *J. Biomed. Opt.* **10**, 044008 (2005).
22. Wang, L. V. & Hu, S. Photoacoustic tomography: in vivo imaging from organelles to organs. *Science* **335**, 1458–1462 (2012).
23. Wang, L. V. & Yao, J. A practical guide to photoacoustic tomography in the life sciences. *Nat. Methods* **13**, 627–638 (2016).
24. Danielli, A. et al. Label-free photoacoustic nanoscopy. *J. Biomed. Opt.* **19**, 086006 (2014).
25. Shi, J., Tang, Y. & Yao, J. Advances in super-resolution photoacoustic imaging. *Quant. Imaging Med. Surg.* **8**, 724–732 (2018).
26. Yao, J., Wang, L., Li, C., Zhang, C. & Wang, L. V. Photoimprint photoacoustic microscopy for three-dimensional label-free subdiffraction imaging. *Phys. Rev. Lett.* **112**, 014302 (2014).
27. Yao, J. et al. High-speed label-free functional photoacoustic microscopy of mouse brain in action. *Nat. Methods* **12**, 407–410 (2015).
28. Li, L. et al. Single-impulse panoramic photoacoustic computed tomography of small-animal whole-body dynamics at high spatiotemporal resolution. *Nat. Biomed. Eng.* **1**, 0071 (2017).
29. Wong, T. T. W. et al. Fast label-free multilayered histology-like imaging of human breast cancer by photoacoustic microscopy. *Sci. Adv.* **3**, e1602168 (2017).
30. Zhang, C., Zhang, Y. S., Yao, D.-K., Xia, Y. & Wang, L. V. Label-free photoacoustic microscopy of cytochromes. *J. Biomed. Opt.* **18**, 020504 (2013).

31. Xu, Z., Li, C. & Wang, L. V. Photoacoustic tomography of water in phantoms and tissue. *J. Biomed. Opt.* **15**, 036019 (2010).
32. Wong, T. T. W. et al. Label-free automated three-dimensional imaging of whole organs by microtomy-assisted photoacoustic microscopy. *Nat. Commun.* **8**, 1386 (2017).
33. Shi, J. et al. High-resolution, high-contrast mid-infrared imaging of fresh biological samples with ultraviolet-localized photoacoustic microscopy. *Nat. Photonics* **13**, 609–615 (2019).
34. Tschuchnig, M. E., Oostingh, G. J. & Gadermayr, M. Generative adversarial networks in digital pathology: a survey on trends and future potential. *Patterns* **1**, 100089 (2020).
35. Rivenon, Y. et al. Virtual histological staining of unlabelled tissue-autofluorescence images via deep learning. *Nat. Biomed. Eng.* **3**, 466–477 (2019).
36. Zhu, J.-Y., Park, T., Isola, P. & Efros, A. A. Unpaired image-to-image translation using cycle-consistent adversarial networks. In *Proceedings of the IEEE international conference on computer vision* 2223–2232 (2017).
37. Lahiani, A. et al. Virtualization of tissue staining in digital pathology using an unsupervised deep learning approach. In *European Congress on Digital Pathology 47–55* (Springer, 2019).
38. Yao, D.-K., Chen, R., Maslov, K., Zhou, Q. & Wang, L. V. Optimal ultraviolet wavelength for in vivo photoacoustic imaging of cell nuclei. *J. Biomed. Opt.* **17**, 056004 (2012).
39. Li, X., Kang, L., Zhang, Y. & Wong, T. T. W. High-speed label-free ultraviolet photoacoustic microscopy for histology-like imaging of unprocessed biological tissues. *Opt. Lett.* **45**, 5401–5404 (2020).
40. Imai, T. et al. High-throughput ultraviolet photoacoustic microscopy with multifocal excitation. *J. Biomed. Opt.* **23**, 036007 (2018).
41. Li, B., Qin, H., Yang, S. & Xing, D. In vivo fast variable focus photoacoustic microscopy using an electrically tunable lens. *Opt. Express* **22**, 20130–20137 (2014).
42. Tang, M., Luo, F. & Liu, D. Automatic time gain compensation in ultrasound imaging system. In *2009 3rd International Conference on Bioinformatics and Biomedical Engineering* 1–4 (IEEE, 2009); <https://doi.org/10.1109/ICBBE.2009.5162432>
43. Xu, Z. et al. Cortex-wide multiparametric photoacoustic microscopy based on real-time contour scanning. *Neurophotonics* **6**, 035012 (2019).
44. Mao, X. et al. Least squares generative adversarial networks. In *Proceedings of the IEEE international conference on computer vision* 2794–2802 (2017).
45. He, K., Zhang, X., Ren, S. & Sun, J. Deep residual learning for image recognition. In *Proceedings of the IEEE conference on computer vision and pattern recognition* 770–778 (2016).
46. Isola, P., Zhu, J.-Y., Zhou, T. & Efros, A. A. Image-to-image translation with conditional adversarial networks. In *Proceedings of the IEEE conference on computer vision and pattern recognition* 1125–1134 (2017).
47. Zhang, R. Making convolutional networks shift-invariant again. In *International conference on machine learning* 7324–7334 (2019).
48. Kingma, D. P. & Ba, J. Adam: a method for stochastic optimization. Preprint at <https://doi.org/10.48550/arXiv.1412.6980> (2017).
49. Humphries, M. P., Maxwell, P. & Salto-Tellez, M. QuPath: the global impact of an open source digital pathology system. *Comput. Struct. Biotechnol. J.* **19**, 852–859 (2021).

Acknowledgements

We thank M. D'Apuzzo for helpful discussions and valuable pathological feedback. This work was sponsored by the United States National Institutes of Health (NIH) grants R01 CA186567 (NIH Director's Transformative Research Award), R35 CA220436 (Outstanding Investigator Award) and R01 EB028277A.

Author contributions

R.C., B.C. and L.V.W. designed the experiment. R.C. and Y.Z. built the system and wrote the control programme. R.C. performed the experiment. S.D.N., B.C. and Y. Liang provided bone specimens and H&E slices. R.C., S.D. and Y. Luo performed image processing. L.V.W. and B.C. supervised the project. All authors were involved in discussions during the work and in the preparation of the manuscript.

Competing interests

L.V.W. has a financial interest in MicroPhotoAcoustics, CalPACT and Union Photoacoustic Technologies. (However, these companies did not financially support this work.) The other authors declare no competing interests.

Additional information

Supplementary information The online version contains supplementary material available at <https://doi.org/10.1038/s41551-022-00940-z>.

Correspondence and requests for materials should be addressed to Brooke Crawford or Lihong V. Wang.

Peer review information *Nature Biomedical Engineering* thanks Ji-Xin Cheng, Carolin Mogler and Ashok Veeraraghavan for their contribution to the peer review of this work.

Reprints and permissions information is available at www.nature.com/reprints.

Publisher's note Springer Nature remains neutral with regard to jurisdictional claims in published maps and institutional affiliations.

Springer Nature or its licensor holds exclusive rights to this article under a publishing agreement with the author(s) or other rightsholder(s); author self-archiving of the accepted manuscript version of this article is solely governed by the terms of such publishing agreement and applicable law.

© The Author(s), under exclusive licence to Springer Nature Limited 2022

Reporting Summary

Nature Portfolio wishes to improve the reproducibility of the work that we publish. This form provides structure for consistency and transparency in reporting. For further information on Nature Portfolio policies, see our [Editorial Policies](#) and the [Editorial Policy Checklist](#).

Statistics

For all statistical analyses, confirm that the following items are present in the figure legend, table legend, main text, or Methods section.

- | n/a | Confirmed |
|-------------------------------------|---|
| <input checked="" type="checkbox"/> | <input type="checkbox"/> The exact sample size (n) for each experimental group/condition, given as a discrete number and unit of measurement |
| <input checked="" type="checkbox"/> | <input type="checkbox"/> A statement on whether measurements were taken from distinct samples or whether the same sample was measured repeatedly |
| <input checked="" type="checkbox"/> | <input type="checkbox"/> The statistical test(s) used AND whether they are one- or two-sided
<i>Only common tests should be described solely by name; describe more complex techniques in the Methods section.</i> |
| <input checked="" type="checkbox"/> | <input type="checkbox"/> A description of all covariates tested |
| <input checked="" type="checkbox"/> | <input type="checkbox"/> A description of any assumptions or corrections, such as tests of normality and adjustment for multiple comparisons |
| <input checked="" type="checkbox"/> | <input type="checkbox"/> A full description of the statistical parameters including central tendency (e.g. means) or other basic estimates (e.g. regression coefficient) AND variation (e.g. standard deviation) or associated estimates of uncertainty (e.g. confidence intervals) |
| <input checked="" type="checkbox"/> | <input type="checkbox"/> For null hypothesis testing, the test statistic (e.g. F , t , r) with confidence intervals, effect sizes, degrees of freedom and P value noted
<i>Give P values as exact values whenever suitable.</i> |
| <input checked="" type="checkbox"/> | <input type="checkbox"/> For Bayesian analysis, information on the choice of priors and Markov chain Monte Carlo settings |
| <input checked="" type="checkbox"/> | <input type="checkbox"/> For hierarchical and complex designs, identification of the appropriate level for tests and full reporting of outcomes |
| <input checked="" type="checkbox"/> | <input type="checkbox"/> Estimates of effect sizes (e.g. Cohen's d , Pearson's r), indicating how they were calculated |

Our web collection on [statistics for biologists](#) contains articles on many of the points above.

Software and code

Policy information about [availability of computer code](#)

Data collection LabVIEW 2015, AlazarTech ATS-VI 5.8.3, Leica Aperio AT2, Matlab.

Data analysis The deep-learning models reported in this work were adapted from code available at <https://github.com/junyanz/pytorch-CycleGAN-and-pix2pix>, which used the PyTorch v1.4.0 (Facebook Inc.) library for Python v3.6. Tiling and stitching procedures were performed using customized Matlab vR2021a codes (The MathWorks Inc.). Training and testing for virtual staining were performed on a graphics processing unit (GPU) node with 4 Nvidia P100 GPUs. The quantitative analysis of photoacoustic virtual histology was done via QuPath (<https://qupath.github.io>).

For manuscripts utilizing custom algorithms or software that are central to the research but not yet described in published literature, software must be made available to editors and reviewers. We strongly encourage code deposition in a community repository (e.g. GitHub). See the Nature Portfolio [guidelines for submitting code & software](#) for further information.

Data

Policy information about [availability of data](#)

All manuscripts must include a [data availability statement](#). This statement should provide the following information, where applicable:

- Accession codes, unique identifiers, or web links for publicly available datasets
- A description of any restrictions on data availability
- For clinical datasets or third party data, please ensure that the statement adheres to our [policy](#)

The main data supporting the findings of this study are available within the paper and its Supplementary Information. The training dataset and the fake output images for the CycleGAN network are available at <https://doi.org/10.5281/zenodo.6345772>. The raw data generated during the study are too large to be publicly shared, yet they are available for research purposes from the corresponding author on reasonable request.

Field-specific reporting

Please select the one below that is the best fit for your research. If you are not sure, read the appropriate sections before making your selection.

Life sciences Behavioural & social sciences Ecological, evolutionary & environmental sciences

For a reference copy of the document with all sections, see [nature.com/documents/nr-reporting-summary-flat.pdf](https://www.nature.com/documents/nr-reporting-summary-flat.pdf)

Life sciences study design

All studies must disclose on these points even when the disclosure is negative.

Sample size	Six unprocessed thick bone specimens and eight bone sections were used to repeat the imaging experiment. No statistical analysis was required. The neural network was trained using data from 2 different tissue samples imaged by PAM and 4 different H&E-stained tissue samples. The PAM and H&E data were split into 89,590 and 133,455 256 x 256 pixel image patches, respectively. These numbers were sufficient to generate virtually stained bone images that cannot be differentiated from H&E images by pathologists.
Data exclusions	No data were excluded.
Replication	All attempts at replication of photoacoustic imaging were successful. After the training of the deep neural networks, they were tested on two tissue slides (composed of 19,065 overlapping 256 x 256 pixel patches); one was tested blindly, the other was included in the training dataset. These were compared to images of corresponding H&E-stained samples.
Randomization	The samples were obtained from the Pathology Core Laboratory on the basis of sample availability. Randomization was not needed for this study.
Blinding	The virtually stained results in this study were performed blindly on data that were not included during the training of the networks. Pathologists were not blinded to sample information.

Reporting for specific materials, systems and methods

We require information from authors about some types of materials, experimental systems and methods used in many studies. Here, indicate whether each material, system or method listed is relevant to your study. If you are not sure if a list item applies to your research, read the appropriate section before selecting a response.

Materials & experimental systems

n/a	Involvement in the study
<input checked="" type="checkbox"/>	<input type="checkbox"/> Antibodies
<input checked="" type="checkbox"/>	<input type="checkbox"/> Eukaryotic cell lines
<input checked="" type="checkbox"/>	<input type="checkbox"/> Palaeontology and archaeology
<input checked="" type="checkbox"/>	<input type="checkbox"/> Animals and other organisms
<input type="checkbox"/>	<input checked="" type="checkbox"/> Human research participants
<input checked="" type="checkbox"/>	<input type="checkbox"/> Clinical data
<input checked="" type="checkbox"/>	<input type="checkbox"/> Dual use research of concern

Methods

n/a	Involvement in the study
<input checked="" type="checkbox"/>	<input type="checkbox"/> ChIP-seq
<input checked="" type="checkbox"/>	<input type="checkbox"/> Flow cytometry
<input checked="" type="checkbox"/>	<input type="checkbox"/> MRI-based neuroimaging

Human research participants

Policy information about [studies involving human research participants](#)

Population characteristics	All the tissue sections used were obtained after de-identification of patient-related information, and were prepared from leftover specimens. Therefore, this work did not interfere with standard practices of care or with sample-collection procedures.
Recruitment	No active recruitment was needed. We used de-identified leftover tissue specimens that had been archived, and therefore that had not been collected specifically for this research.
Ethics oversight	All experiments and protocols used in the study were approved by the Institutional Review Boards at the California Institute of Technology, the University of California at Los Angeles, and the City of Hope.

Note that full information on the approval of the study protocol must also be provided in the manuscript.